Marvin, M.C., et al., 2023, Dune interactions record changes in boundary conditions: Geology, https://doi.org/10.1130/G51264.1

Supplemental Material

Supplemental text describing methods for dune-field digitization, digitization sensitivity analysis, sediment flux calculations, and turnover time scales; validation for turnover time scales; terrestrial wind data sensitivity analysis; three supplemental tables and five figures; and all compiled data.

Supplementary Material for "Dune interactions record changes in boundary conditions"

Marvin, M. C. [1*], Lapôtre, M. G. A.[1], Gunn, A.[2], Day, M.[3], Soto, A.[4]

[1] *Department of Earth and Planetary Sciences, Stanford University, Stanford, CA, 94305, USA*

[2] *Department of Earth, Planetary, and Space Sciences, University of California Los Angeles, Los Angeles, CA 90095, USA*

[3] *School of Earth, Atmosphere & Environment, Monash University, Clayton, VIC, 3800, Australia*

[4] *Department of Space Studies, Southwest Research Institute, Boulder, CO, USA*

[*] *Email: mcmarvin@stanford.edu*

This file contains:
Supplementary Text
Supplementary References
Supplementary Tables S1–S3 and caption of Supplementary Table S4
Supplementary Figures S1–S3

SUPPLEMENTARY TEXT

Updated Counting Methodology

We use a similar but updated methodology to that of Day & Kocurek (2018) to quantify interaction density. Through an analysis of 32 dune fields on Earth, Mars, and Titan, Day & Kocurek (2018) showed that

$$I = \alpha\lambda^{-2}, \quad (1)$$

where λ is dune spacing, regardless of dune type (crescentic vs. linear), but found that the proportionality constant, α, was different for crescentic (α = 0.58) and linear (α = 0.04) dunes. To calculate I, previous studies defined a rectangular counting area, the dimensions of which were fixed to be some multiple of mean dune spacing ($m_1\lambda$ and $m_2\lambda$), such that the surface area of the counting polygon was given by

$$A \sim m_1 m_2 \lambda^2. \quad (2)$$

For fields of crescentic dunes, square counting polygons ($m_1 = m_2$) were used, such that $A_{\text{crescentic}} = {m_1}^2\lambda^2$. In contrast, counting polygons with $m_1 \neq m_2$ were used over fields of linear dunes in order to capture enough interactions within the polygon, such that

$$I_{\text{crescentic}} \sim \frac{n}{{m_1}^2}\lambda^{-2} \quad (3)$$

whereas

$$I_{\text{linear}} \sim \frac{n}{m_1 m_2}\lambda^{-2}. \quad (4)$$

Comparing Eqs. 3–4 to Eq. 1, it becomes apparent that the different prefactors, α, determined by Day & Kocurek (2018) could in principle arise from methodology rather than reflect a true distinction between crescentic and linear dunes.

To decouple the dimensions of counting areas from both dune type and dune spacing, we identified the largest region within a dune field where dune spacing was roughly homogenous (of area, A_{h}), and generated a circular counting area of surface area $A = A_{\text{h}}/2$ within that region (Figure S1A). Thus, A is largely controlled by dune field extent rather than average dune dimension.

Dune-Field Digitization and Pattern Parameters

All dune field digitization was done in QGIS 3.16 *Hannover*. The ESRI satellite in the WGS 84/Pseudo-Mercator projection (EPSG:3857) was used for all terrestrial dune sites but the Tengger Desert site. The ESRI base map utilizes Maxar imagery at 0.5 m/pixel resolution over the United States and SPOT imagery with 2.5 m/pixel resolution worldwide. For the Tengger Desert site, Google Earth Pro historical imagery was used as repeat imagery and higher resolution were required to capture the time evolution of smaller, nascent dunes. Three control points were imported into Google Earth Pro and exported as a part of each historical image. Then, the same control points in QGIS were tied to the control points in the image to georeference each image, in the WGS 84/UTM Zone 84N projection (EPSG:32648). Martian dune sites were digitized on Context Camera (CTX; Malin et al., 2007) tiles at 5 m/pixel from the Dickson et al. (2018) mosaic. Tiles were cylindrically projected around the nearest parallel and were coupled with the Mars 2000 IAU IAG ellipsoid.

Dune crestlines were then traced manually following the methodology of Ewing et al. (2006). Crescentic crestlines were traced along the top of slipfaces, whereas linear crestlines, which lack slipfaces, were traced from end to end. Although dune crestlines can in principle be mapped automatically using traditional image processing or machine learning approaches (e.g., Rubanenko et al., 2021), (i) machine learning would require substantial manual tracing for training data in the first place, (ii) mapping precision would vary from scene to scene, and thus, the detection rate of dune interactions could also vary from scene to scene, and (iii) our total dataset size (n=46) is not large enough to make a performant automated approach faster than a manual one. Manual tracing allows us to minimize error and keep any biases consistent throughout so dune fields can be compared against each other.

Next, 20–50 random points were generated depending on counting area (e.g., ~20 for $A <$ 1 km^2, 30 for $1 < A < 100$ km^2, 40 for $100 < A < 1000$ km^2, and 50 for $A > 1000$ km^2). Average dune spacing, λ, was calculated as the mean distance between the two dune crests closest to those points. Following the definition of Day & Kocurek (2018), interactions were defined as locations where dune crestlines are within 0.1λ from each other. To identify interactions, buffers were generated at a distance 0.05λ around dune crestlines, such that intersecting buffers indicate dune interactions (Figure S1B). Upon counting the number of interactions, n, within the counting area, we calculated, I and I_*, as well as measured the average crestline azimuth within the counting area, δ_d, using the azimuth function in QGIS. This procedure estimates the crestline orientation of each dune as approximated by a line connecting the crestline endpoints, from which the field-average orientation can be determined. Finally, the total dune length, L_d, and for crescentic dunes, the planform slipface length, L_s, were measured for dunes closest to the randomly generated points.

Digitization and Pattern Parameter Sensitivity Analysis

To assess the sensitivity of our results to methodological choices, we conducted a sensitivity analysis. Three terrestrial dune fields with small (97.8 m), medium (1014 m), and large (2465 m) dune spacings were selected for analysis. At each site, we compared our baseline interaction statistics with those obtained when (i) the surface area of the original counting circle was doubled ('A2' in Fig. S4–5), (ii) the center of the counting circle was shifted laterally while roughly maintaining its size ('adjacent' in Fig. S4–5), and (iii) the threshold length scale used to define a dune interaction was halved (0.05λ) and doubled (0.2λ), respectively (0.05λ and 0.2λ in Fig. S4,5). Intuitively, we find that altering the definition of a dune interaction induces the most variability (by up to ~100%). In contrast, changing the size of the counting area or specific location

only slightly alters the results quantitatively (Fig. S4–5). We find that uncertainty is less than a factor of 1 for all digitization variations. When the definition of an interaction is kept constant, we find that typical uncertainties are typically bracketed by [0.7 1.8]I (and [0.7 1.8]I_*), which we adopt as conservative error bars in all plots of I and I_*.

Sediment Flux

Wind data for Earth were collected from the ERA5-Land dataset (Muñoz Sabater, 2019) between 1992 and 2021 with a grid size of ~9 km. ERA5-Land wind data were queried to interpolate wind from the 'nearest' grid point to each specific site. For Mars, wind data were derived from a MarsWRF simulation (Richardson et al., 2007) run for one martian year (669 Earth days) with a 5×5° grid size. The same simulation setup as Rivera-Valentín et al. (2020) and Chevrier et al. (2020) was used for the MarsWRF simulation, with a non-prescribed dust scheme, a CO2 cycle, and a water cycle that included radiatively active water and dust (Lee et al., 2018). Determining uncertainty from MarsWRF is beyond the scope of this work, but the reader is directed to the literature for previous work (i.e., Richardson et al., 2007 and subsequent works). Regardless, the MarsWRF data provides a strong foundation from which to conduct our analysis.

Both ERA5-Land and MarsWRF output instantaneous, hourly atmospheric density, ρ_f, and the longitudinal and latitudinal components of wind velocity at a height z =10 m above ground (u_{10} and v_{10}, respectively). We used a constant value of atmospheric density for Earth (Table S1), whereas local and instantaneous atmospheric density values were used on Mars due to its higher variability. Wind speed magnitude (U_{10}) and resultant drift direction (δ_w) were calculated as $U_{10} = \sqrt{u_{10}^2 + v_{10}^2}$ and $\delta_w = \arctan(v_{10}/u_{10})$, respectively.

Sand is mobilized when wind shear velocity, u_*, exceeds a threshold value. Shear velocity was calculated from U_{10} using the law of the wall as $u_* = (\kappa U_{10})/\ln(z/z_0)$, where κ = 0.4 is the von Karman constant, z = 10 m, and z_0 encapsulates information about roughness height of the bed (Table S1). For Earth, we employed the impact threshold equation of Bagnold (1941),

$$u_{*\mathrm{it}} = 0.082\sqrt{\frac{\rho_\mathrm{s} - \rho_\mathrm{f}}{\rho_\mathrm{f}} g d}, \tag{5}$$

where ρ_s and ρ_f are the densities of sediment and the atmosphere, respectively, $g = 9.81$ m/s^2 is the acceleration of gravity, and $d = 300$ μm is grain diameter. On Mars, threshold shear velocity values for the initiation and continuation of saltation (the fluid and impact thresholds, respectively) have been proposed from a combination of theory and wind tunnel experiments (Swann et al., 2020; Andreotti et al., 2021; Gunn & Jerolmack, 2022). Here, we used a value derived from repeat satellite imagery of a martian dune field and that applies to modeling sand fluxes at the landscape scale (Ayoub et al., 2014).

Next, we estimated the saturated mass flux, q, following the formulation of Martin & Kok (2017), as

$$q = \gamma \frac{\rho_f u_{*,it}}{g}({u_*}^2 - {u_{*,it}}^2) \tag{6}$$

where γ = 5. Flux was projected along the net-dune migration direction,

$$q_\mathrm{m} = q \times |f(\delta_\mathrm{w} - \delta_\mathrm{d})|, \tag{7}$$

where $f = \cos$ for transverse dunes, $f = \sin$ for longitudinal dunes, and δ_d is the azimuth of the dune crestline. Finally, the saturated volume flux at the crest, $q_\mathrm{m,c}$, was estimated from q_m taking into account the acceleration of winds up dune slopes. Specifically, we estimated the flux at the crest as

$$q_\mathrm{m,c} = q_\mathrm{m}(1 + \beta S), \tag{8}$$

where $\beta \sim 9.4$ is a speed up factor (Courrech du Pont et al., 2014; Gunn, 2022) and S is bed slope upwind of the crest as measured in the flux direction. Thus, assuming that the flux at the dune toe is negligible (~0), the average sand flux can be estimated as

$$\bar{q} = \frac{q_{m,c}}{2}. \tag{9}$$

Because Equation 6 was calibrated for saltation under terrestrial conditions (Martin & Kok, 2017), we empirically corrected our martian fluxes as

$$\bar{q}_{\text{corrected}} = c_{\text{NP}} \bar{q}_{\text{modeled}}, \tag{10}$$

where c_{NP} is a correction factor determined using previously constrained sand fluxes at Nili Patera, and $\bar{q}_{\text{modeled}}$ is the average sand flux as determined from Equation 6 and MarsWRF outputs. Through correlation of repeat high-resolution imagery, Bridges et al. (2012) estimated (from dune size and migration rate) that the width-averaged volumetric sand flux was ~2.3 m^2/Earth year at Nili Patera. In contrast, combining Equation 6 and MarsWRF outputs for our two Nili Patera locations yields saturated average sand fluxes of ~7.4 and ~5.3 m^2/Earth year, respectively. We thus calculated a correction factor, c_{NP}, such that it would minimize the mismatch between the flux as estimated by Bridges et al. (2012) and our two modeled values,

$$c_{\text{NP}} = \frac{\bar{q}_{\text{NP,B2012}}}{\bar{q}_{\text{NP,modeled}}} \approx 0.36, \tag{11}$$

where $\bar{q}_{\text{NP,B2012}}$= 2.3 m^2/Earth year and $\bar{q}_{\text{NP,modeled}} = \frac{7.4+5.3}{2} = 6.4$ m^2/Earth year.

Turnover Timescales

The turnover timescale, T_{t} (which can be used a s proxy for the timescale of dune adjustment) is a function of dune size and sediment flux (Allen, 1974, 1976; Myrow et al., 2018). We calculate T_{t} as

$$T_{\text{t}} = \frac{A_{\text{dune}}}{\bar{q}}, \tag{12}$$

where $A_{\mathrm{dune}}$is the dune cross-sectional area along its migration direction. We approximated dune cross-sectional area as a triangle such that

$$A_{\mathrm{dune}} = \frac{L_{\mathrm{d}} H}{2}, \tag{13}$$

where L_{d} and H are dune length and height, respectively. For crescentic dunes, dune height was calculated as

$$H_{\mathrm{crescentic}} = L_{\mathrm{s}} \tan\theta\,, \tag{14}$$

where L_{s} is the planform slipface length and $\theta \approx 30°$ is the angle of repose of dry cohesionless sand. The height of linear dunes was measured from SRTM rasters (30 m/pixel) accessed via Google Earth Engine (Farr et al., 2007) with the exception of the Rice Valley dune site. At Rice Valley, we used elevation data derived from aerial lidar at 1 m/pixel collected by the National Center for Aerial Laser Mapping (NCALM). In QGIS, a transect was drawn across the whole counting area in the dune-crest-normal direction, from which a vector of elevation values was derived. Only the middle 96% of the transect was used to avoid edge effects. A line was fit to the elevation profile using a linear regression and subtracted from the overall profile to remove the topographic signature of sloping terrains. From flattened profiles (z), we calculated dune height as

$$H_{\mathrm{linear}} = 2\sqrt{\mathrm{mean}(z^2)}. \tag{15}$$

Finally, turnover times were calculated from Equation 3 in the main text, assuming $\varphi = 0.3$.

Validating Calculated Turnover Timescales

To ensure robustness of calculated turnover timescales despite simplifications and assumptions, we sought to validate our approach by comparing our estimates with independent constraints where available. Many previous studies provide dune migration rate rather than a turnover timescale. Thus, we compared published dune migration rates with

$$M_{\mathrm{r}} = \frac{L_{\mathrm{d}}}{T_{\mathrm{t}}}, \tag{16}$$

as derived in this study (Table S2).

For dune fields that have been active for a longer time than the turnover time of its dunes, our model performs particularly well regardless of dune type. However, our approach relies on the assumption of unlimited sand supply and availability (i.e., no vegetation, cohesive crusts, ice, etc.). Thus, our calculated turnover times for stabilized dune fields (such as vegetated linear dunes in Australia and the Kalahari Desert as well as ice-covered barchans in Olympia Undae on Mars) are only representative of what they would be in the absence of these stabilizing agents. Dune stabilization increases true turnover timescale, such that our estimates provide lower bounds in such cases. Correcting for the effect of dune stabilization on turnover timescale would not alter our conclusions. However, the interaction index of stabilized dune patterns may lag significantly, possibly even representing its value at the time of stabilization (Figure S2). In addition, we have added error bars of [0.2 4.3]T_{t} to Fig. 4A in the main text and Fig. S2 derived from a comparison of our derived T_{t} and M_{r} values from the literature (Table S2). The maximum relative error is specifically in reference to the minimum bound of migration rates of dunes at Nili Patera (0.03 m Earth yr^{-1} Bridges et al., 2012) relative to our migration rate of 0.16 m Earth yr^{-1}. Our values are well within the ranges of T_{t} and M_{r} values. The error bars represent very conservative values: most T_{t} and M_{r} values are < +/- ~35% when compared with values from the literature.

Data Compilation

All compiled data for the 46 investigated sites are provided in Table S4 as a supplementary .csv file.

Sensitivity Analysis: Comparison Between ERA5-Land and ERA5 Wind Data

To assess the sensitivity of our results to the choice of wind data, we conducted the same analysis using both ERA5 and ERA5-Land hourly data provided by the European Centre for Medium-Range Weather Forecasts (ECMRWF). Each datasets provides instantaneous latitudinal and longitudinal wind vectors at an elevation of 10 m at ~30 km (ERA5) and ~9 km (ERA5-Land) grid sizes (Muñoz Sabater, 2019; Hersbach et al., 2020). Figure S3 shows a comparison of calculated saturated mass flux (q), resultant drift direction (δ_{w}), and resultant drift potential normalized by drift potential (RDP/DP) from both datasets. Small discrepancies between the two datasets are present but minimal. We chose to employ ERA5-Land data owing to its finer grid scale, allowing us to estimate sand fluxes closer to our specific sites and to draw more direct comparisons of estimated dune turnover timescales with previously published independent constraints (Table S2).

REFERENCES CITED

Allen, J.R.L., 1974, Reaction, relaxation and lag in natural sedimentary systems: General principles, examples and lessons: Earth-Science Reviews, v. 10, p. 263–342, doi:10.1016/0012-8252(74)90109-3.

Allen, J.R.L., 1976, Time-lag of dunes in unsteady flows: An analysis of Nasner's data from the R. Weser, Germany: Sedimentary Geology, v. 15, p. 309–321, doi:10.1016/0037-0738(76)90037-3.

Andreotti, B., Claudin, P., Iversen, J.J., Merrison, J.P., and Rasmussen, K.R., 2021, A lower-than-expected saltation threshold at Martian pressure and below: Proceedings of the National Academy of Sciences, v. 118, p. e2012386118, doi:10.1073/pnas.2012386118.

Ayoub, F., Avouac, J.-P., Newman, C.E., Richardson, M.I., Lucas, A., Leprince, S., and Bridges, N.T., 2014, Threshold for sand mobility on Mars calibrated from seasonal variations of sand flux: Nature Communications, v. 5, p. 5096, doi:10.1038/ncomms6096.

Bagnold, R. A. (1941). The physics of blown sand and desert dunes. Courier Corporation.

Bridges, N.T., Ayoub, F., Avouac, J.-P., Leprince, S., Lucas, A., and Mattson, S., 2012, Earth-like sand fluxes on Mars: Nature, v. 485, p. 339–342, doi:10.1038/nature11022.

Bridges, N.T. et al., 2017, Martian aeolian activity at the Bagnold Dunes, Gale Crater: The view from the surface and orbit: Aeolian Activity at the Bagnold Dunes: Journal of Geophysical Research: Planets, v. 122, p. 2077–2110, doi:10.1002/2017JE005263.

Bristow, C.S., Duller, G.A.T., and Lancaster, N., 2007, Age and dynamics of linear dunes in the Namib Desert: Geology, v. 35, p. 555, doi:10.1130/G23369A.1.

Chevrier, V.F., Rivera-Valentín, E.G., Soto, A., and Altheide, T.S., 2020, Global Temporal and Geographic Stability of Brines on Present-day Mars: The Planetary Science Journal, v. 1, p. 64, doi:10.3847/PSJ/abbc14.

Chojnacki, M., Banks, M.E., Fenton, L.K., and Urso, A.C., 2019, Boundary condition controls on the high-sand-flux regions of Mars: Geology, v. 47, p. 427–430, doi:10.1130/G45793.1.

Day, M., and Kocurek, G., 2018, Pattern similarity across planetary dune fields: Geology, v. 46, p. 999–1002, doi:10.1130/G45547.1.

Dickson, J.L., Kerber, L., Fassett, C.I., and Ehlmann, B.L., 2018, A global, blended CTX mosaic of Mars with vectorized seam mapping: A new mosaicking pipeline using principles of non-destructive image editing: Abstract 2840 presented at the 49th Lunar and Planetary Science Conference, The Woodlands, Texas, 19–23 March.

Farr, T.G. et al., 2007, The Shuttle Radar Topography Mission: Reviews of Geophysics, v. 45, p. RG2004, doi:10.1029/2005RG000183.

Farrant, A.R., Duller, G.A.T., Parker, A.G., Roberts, H.M., Parton, A., Knox, R.W.O., and Bide, T., 2015, Developing a framework of Quaternary dune accumulation in the northern Rub' al-Khali, Arabia: Quaternary International, v. 382, p. 132–144, doi:10.1016/j.quaint.2015.02.022.

Gunn, A., and Jerolmack, D.J., 2022, Conditions for aeolian transport in the Solar System: Nature Astronomy, v. 6, p. 923–929, doi:10.1038/s41550-022-01669-0.

Hersbach, H. et al., 2020, The ERA5 global reanalysis: Quarterly Journal of the Royal Meteorological Society, v. 146, p. 1999–2049, doi:10.1002/qj.3803.

Hoover, R.H., Gaylord, D.R., and Cooper, C.M., 2018, Dune mobility in the St. Anthony Dune Field, Idaho, USA: Effects of meteorological variables and lag time: Geomorphology, v. 309, p. 29–37, doi:10.1016/j.geomorph.2018.02.018.

Lee, C., Richardson, M.I., Newman, C.E., and Mischna, M.A., 2018, The sensitivity of solsticial pauses to atmospheric ice and dust in the MarsWRF General Circulation Model: Icarus, v. 311, p. 23–34, doi:10.1016/j.icarus.2018.03.019.

Malin, M.C. et al., 2007, Context Camera Investigation on board the Mars Reconnaissance Orbiter: Journal of Geophysical Research, v. 112, p. E05S04, doi:10.1029/2006JE002808.

Muñoz Sabater, J., (2019): ERA5-Land hourly data from 1981 to present: Copernicus Climate Change Service (C3S) Climate Data Store (CDS). (Accessed on 24-02-2023), doi: 10.24381/cds.e2161bac.

Myrow, P.M., Jerolmack, D.J., and Perron, J.T., 2018, Bedform Disequilibrium: Journal of Sedimentary Research, v. 88, p. L19402, doi:10.2110/jsr.2018.55.

Richardson, M.I., Toigo, A.D., and Newman, C.E., 2007, PlanetWRF: A general purpose, local to global numerical model for planetary atmospheric and climate dynamics: Journal of Geophysical Research, v. 112, p. E09001, doi:10.1029/2006JE002825.

Rivera-Valentín, E.G., Chevrier, V.F., Soto, A., and Martínez, G., 2020, Distribution and habitability of (meta)stable brines on present-day Mars: Nature Astronomy, v. 4, p. 756–761, doi:10.1038/s41550-020-1080-9.

Rubanenko, L., Perez-Lopez, S., Schull, J., and Lapôtre, M.G.A., 2021, Automatic Detection and Segmentation of Barchan Dunes on Mars and Earth Using a Convolutional Neural Network: IEEE Journal of Selected Topics in Applied Earth Observations and Remote Sensing, v. 14, p. 9364–9371, doi:10.1109/JSTARS.2021.3109900.

Swann, C., Sherman, D.J., and Ewing, R.C., 2020, Experimentally Derived Thresholds for Windblown Sand on Mars: Geophysical Research Letters, v. 47, doi:10.1029/2019GL084484.

SUPPLEMENTARY TABLES

Table S1. Environmental parameters used in Eq. 9 for Earth and Mars. Roughness heights for Earth and Mars from Gunn (2023) and Bridges et al. (2017), respectively.

Planet	Grain diameter, d (m)	Height above the bed, z (m)	Gravitational acceleration, g (m/s^2)	Roughness height, z_0 (m)	Sediment density, ρ_f (kg/m^3)	Atmospheric density, ρ_s (kg/m^3)
Earth	3.0 x 10^{-4}	10	9.8	1.0 x 10^{-3}	2650	1.2
Mars	3.0 x 10^{-4}	10	3.7	1.0 x 10^{-4}	3000	from MarsWRF

Table S2. Comparison of turnover timescales or dune migration rates (Mr) from this study and previously published, independent constraints.

Site	Planet	Type	Mr, this study (m/Earth yr)	Mr, reference, (m/Earth yr)	T_t, this study (Earth yr)	T_t, reference, (Earth yr)	Reference
Nili Patera	Mars	Crescentic	0.16, 0.22	0.03-0.27	1688, 2013	n/a	Bridges et al. (2012)
Kaiser Crater	Mars	Crescentic	0.40	0.60	894	n/a	Chojnacki et al. (2019)
White Sands	Earth	Crescentic	0.69	n/a	135	100	Myrow et al. (2018)
St. Anthony's, Idaho	Earth	Crescentic	1.1	1.0-1.8	41	n/a	Hoover et al. (2018)
Rub 'al Khali	Earth	Crescentic	0.1	n/a	15358	10000	Farrant et al. (2015)
Namib	Earth	Linear	0.1	0.1	8350	n/a	Bristow et al. (2007)

Table S3. Description of variables in Table S4.

Variable	Unit	Description
NAME	n/a	counting area name
SITENAME	n/a	same as NAME, except for counting areas along a transect or digitized through time
LAT	decimal degrees	latitude
LONG	decimal degrees	longitude
IMAGE_DATE	YYYYMMDD	date of google earth historical imagery
SITE_ID	n/a	counting area ID
ALL_ID	n/a	overall ID
TYPE	n/a	crescentic or linear dune
ENVIRONMENT	n/a	fluvial or aeolian dune
BODY	n/a	Mars or Earth
STABILIZED	n/a	is the dune field stabilized or not?
LOWER_BOUND_FIG2	n/a	was this site used to calculate the observed lower bound in Fig. 2?
LOWER_BOUND_FIG4	n/a	was this site used to calculate the observed lower bound in Fig. 4?
AREA_M2	m^2	area of counting circle
DIST_DOWNWIND_M	m	distance downwind from starting point; only for dunes along a transect
TOT_DUNE	integer	number of individual crestlines that intersect the counting area
NUM_INT	integer	number of interactions
LAMBDA_M	m	average dune spacing
LAMBDA_M_SD	m	standard deviation of dune spacing
SLIP_M	m	average slipface length
Ld_M	m	average dune length
stoss	dimensionless	stoss slope, H / Ld_M
AZIMUTH_MEAN	radian	average crestline orientation (N of E)
H	m	height of dune
qm	kg m^{-1} s^{-1}	saturated flux (RDP)
qa	radian	net flux angle (RDD) (N of E)

q	$m^2\ yr^{-1}$	average flux dune across dune
RDP_DP	dimensionless	ratio of RDP / DP, proxy for wind variability
Tt	yr	turnover time
Mr	$m\ yr^{-1}$	migration rate normal to crest
I_M2	m^2	interaction density, I
Istar	dimensionless	interaction index, I*

Table S4. Data compilation from 46 dune fields on Earth and Mars (provided as a supplementary .csv file).

Table S5. Data compilation of our digitization sensitivity analysis comparing average dune spacing, counting area size, interaction density, and interaction index (and their corresponding errors). The last two columns report the ratio of I (or I_*) as calculated through a given analysis type and I (or I_*) as calculated through our 'original", baseline analysis.

Site Name	Analysis Type	Interactions (n)	Average Dune Spacing (m)	Counting Area, A (m^2)	Interaction Density, I (m^{-2})	Interaction Index (I_*)	I Ratio	I_* Ratio
Grand Erg Linear	Original	9	2465.2	1.11E+09	8.09E-09	4.92E-02	1	1
Gibson	Original	36	1014	2.41E+08	1.49E-07	1.54E-01	1	1
Little Sahara, Utah	Original	20	97.8	1.23E+06	1.63E-05	1.56E-01	1	1
Grand Erg Linear	2x area	10	2465.2	2.23E+09	4.49E-09	2.73E-02	0.56	0.56
Gibson	2x area	66	1014	4.82E+08	1.37E-07	1.41E-01	0.92	0.92
Little Sahara, Utah	2x area	28	97.8	2.46E+06	1.14E-05	1.09E-01	0.7	0.7
Grand Erg Linear	Adjacent to original counting area	2	2482.7	8.42E+08	2.38E-09	1.46E-02	0.29	0.3
Gibson	Adjacent to original counting area	43	833.61	2.07E+08	2.07E-07	1.44E-01	1.39	0.94

Little Sahara, Utah	Adjacent to original counting area	7	89.7	7.14E+05	9.80E-06	7.89E-02	0.6	0.51
Grand Erg Linear	Original, 0.05λ buffer	8	2465.2	1.11E+09	7.19E-09	4.37E-02	0.89	0.89
Gibson	Original, 0.05λ buffer	35	1014	2.41E+08	1.45E-07	1.49E-01	0.97	0.97
Little Sahara, Utah	Original, 0.05λ buffer	6	97.8	1.23E+06	4.88E-06	4.67E-02	0.3	0.3
Grand Erg Linear	Original, 0.2λ buffer	9	2465.2	1.11E+09	8.09E-09	4.92E-02	1	1
Gibson	Original, 0.2λ buffer	42	1014	2.41E+08	1.74E-07	1.79E-01	1.17	1.17
Little Sahara, Utah	Original, 0.2λ buffer	44	97.8	1.23E+06	3.58E-05	3.42E-01	2.2	2.2

SUPPLEMENTARY FIGURES

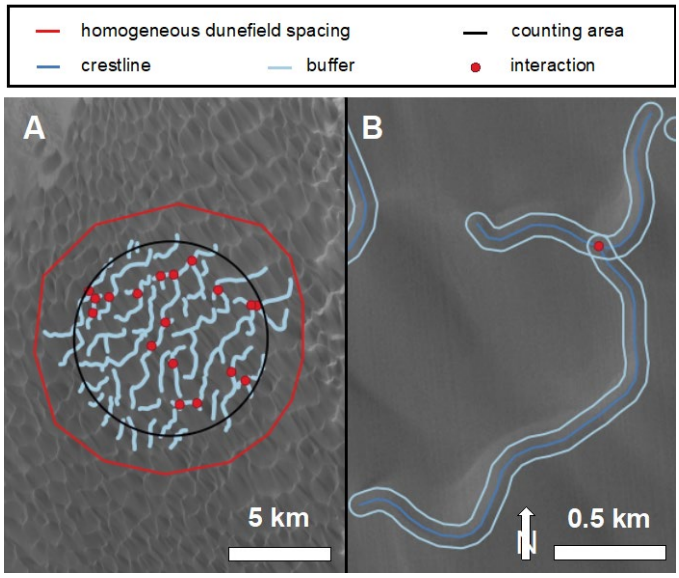

Figure S1. (A) Digitized counting area at Rabe Crater on Mars. (B) Zoomed in display showing buffers of 0.05λ generated around dune crestlines. Basemap from Dickson et al. (2018) mosaic.

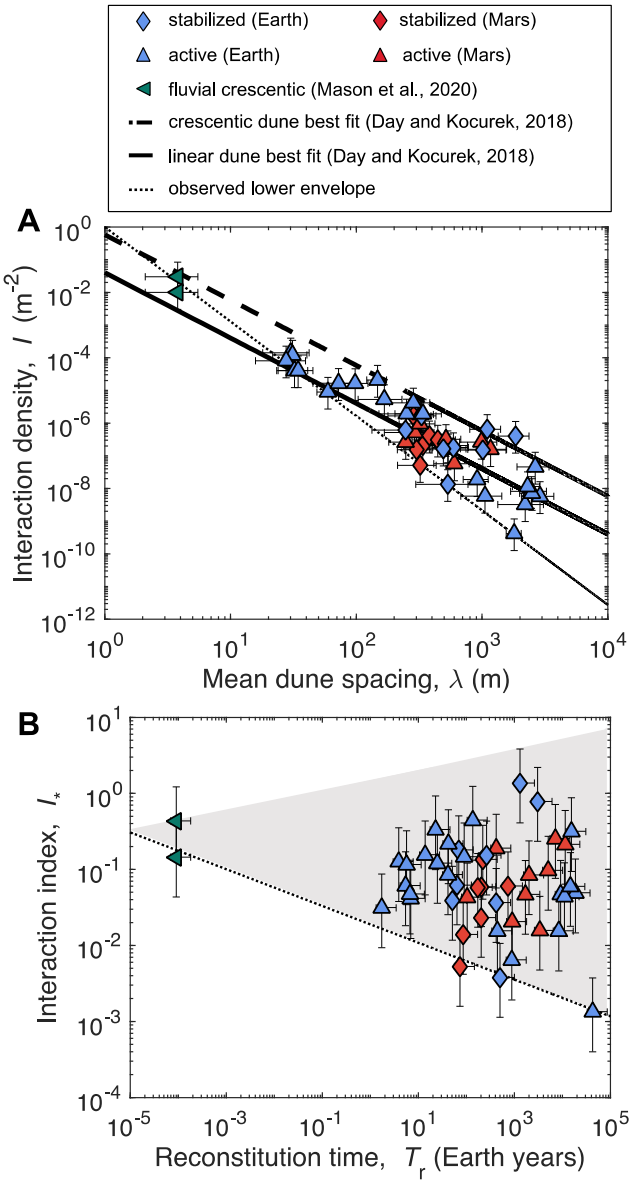

Figure S2. (A) Quadratic decrease in interaction density with increasing dune spacing for 46 fields of linear and crescentic dunes on Earth and Mars (same as Fig. 2A) and (B) dune interaction index as a function of dune turnover timescale on Earth (same as Fig. 4A) highlighting stabilized and active dune-fields.

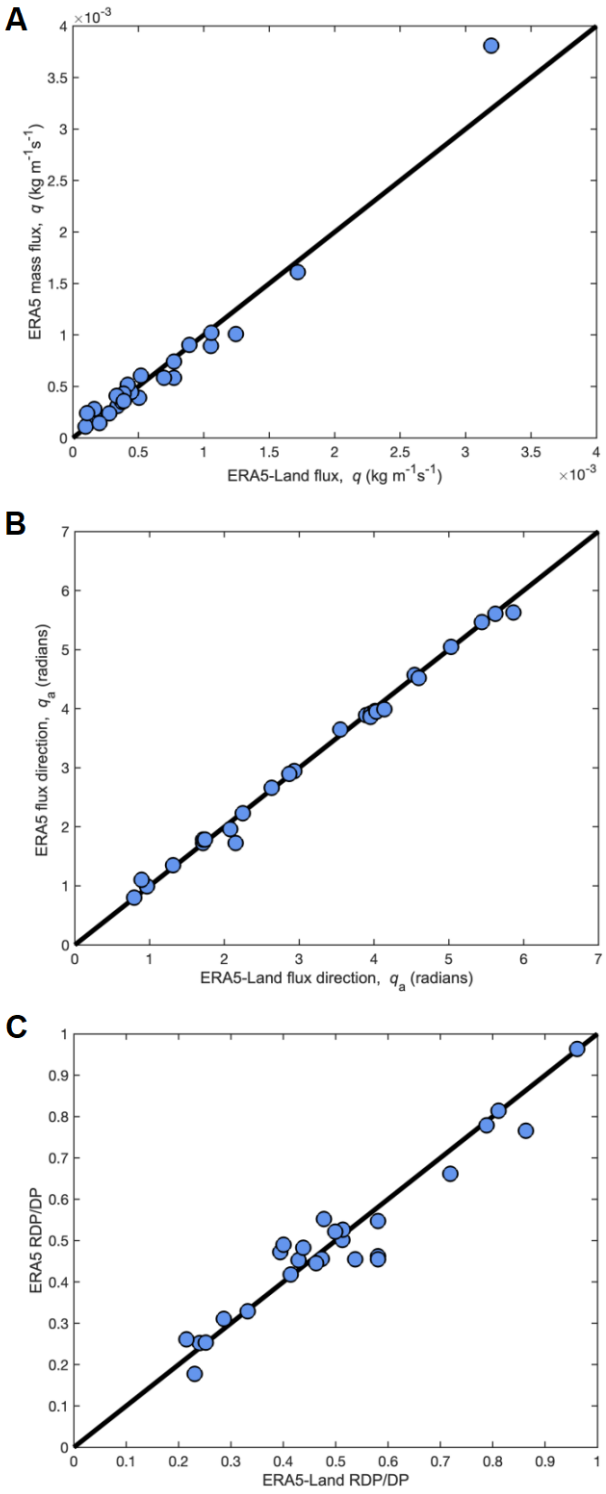

Figure S3. Comparison of (A) saturated mass flux, (B) resultant drift direction, and (C) RDP/DP derived from ERA5 and ERA5-Land data.

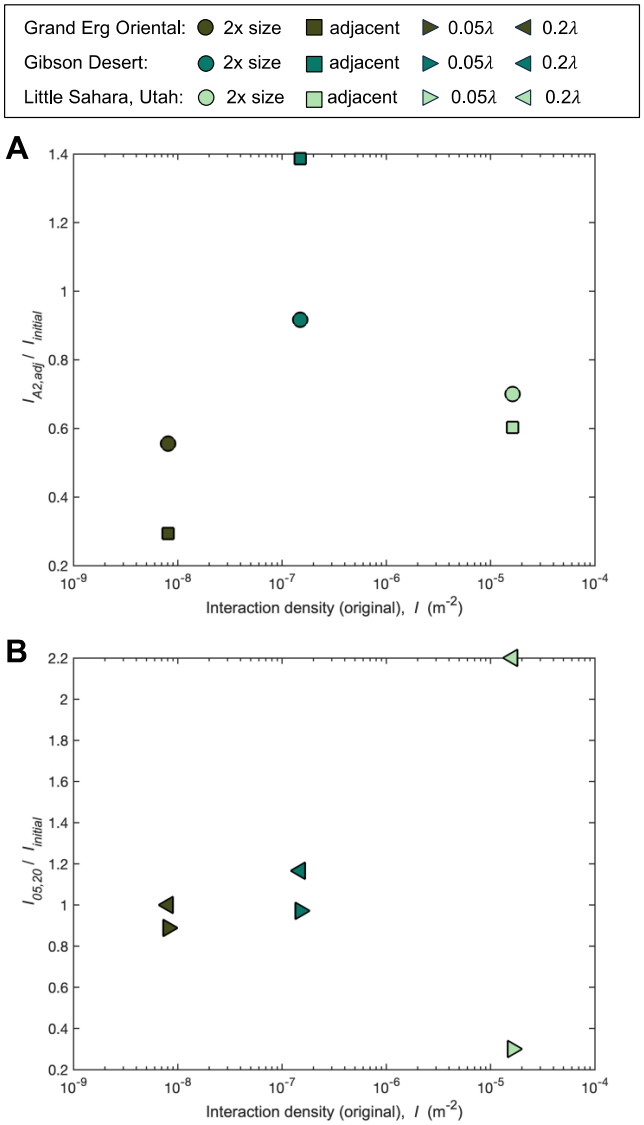

Figure S4. Comparison of I as determined using our baseline methodology and (A) counting areas of 2x the original size and adjacent, similarly sized counting areas, and (B) keeping the original counting area the same but changing the crestline buffer sizes such that interactions are counted when dunes are $<0.05\lambda$ or $<0.2\lambda$ apart. This corresponds to 0.025λ and $0.1\ \lambda$ buffer sizes (half and double the size of the original $0.05\ \lambda$ buffers used to determine dunes $<0.1\lambda$ apart).

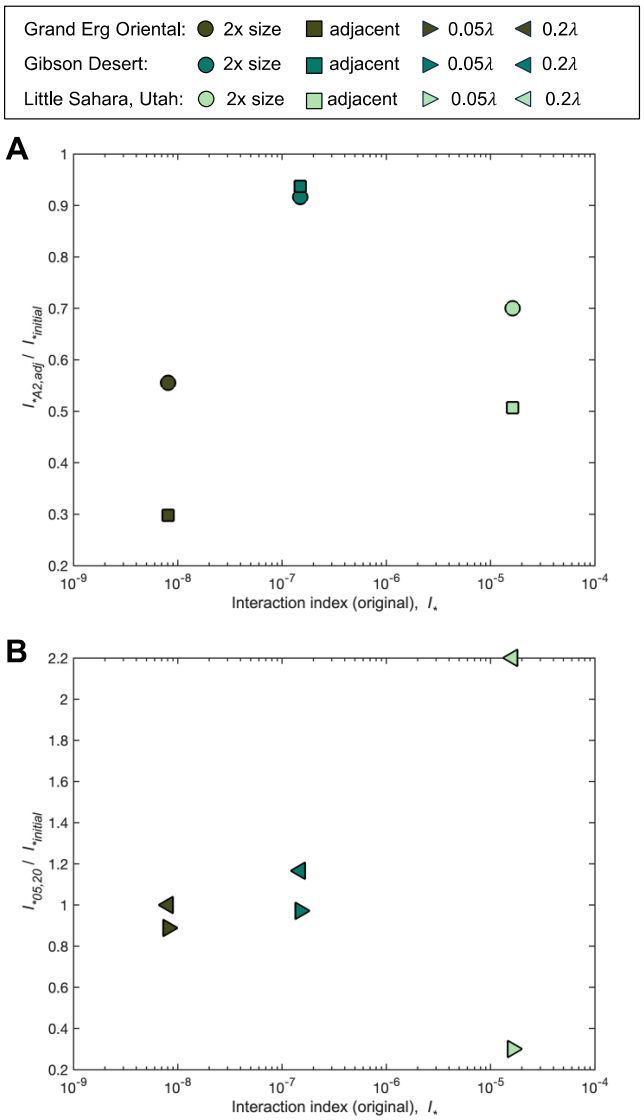

Figure S5. Comparison of I_* as determined using our baseline methodology and (A) counting areas of 2x the original size and adjacent, similarly sized counting areas, and (B) keeping the original counting area the same but changing the crestline buffer sizes such that interactions are counted when dunes are <0.05λ or <0.2λ apart. This corresponds to 0.025λ and 0.1 λ buffer sizes (half and double the size of the original 0.05 λ buffers used to determine dunes <0.1λ apart).